

Shape Memory Soft Robotics with Yield Stress Fluids

Jackson Kyle Wilt,* Johannes T. B. Overvelde, and Corentin Coulais

Biological movement is a source of inspiration for designing soft robots that use fluidic actuation for adaptive gripping and locomotion. While many biological systems use networks of non-Newtonian fluid for movement, to date, most soft robots use Newtonian fluids or pneumatics. Herein, yield stress fluids to manufacture and operate soft devices are exploited, particularly to create soft actuators that exhibit shape memory. Our soft robots are fabricated through embedded 3D printing where the suspension media is a yield stress fluid. Moreover, this complex fluid is encapsulated and used as the hydraulic transmission fluid. Diagnostic designs are developed to characterize the force and shape memory of the yield stress fluid, and the findings are used to create a gripper common in modern soft robotic applications. The diagnostic devices have deformable reservoirs that demonstrate force response, flow behavior, and deformation profiles dependent on the yield stress features of the transmission fluid. The actuation using the yield stress fluid from the retained suspension media creates avenues for partial shape retention and unconventional expansion from localized fluid flow. Looking toward the future of soft robotics, these fabrication and operational approaches using yield stress fluids can provide greater tunability for applications requiring nonlinear actuation and shape memory.

1. Introduction

Soft robotics is becoming a mainstay of the automation toolbox due to their plethora of applications in human-computer interfaces, implantable devices, and grasping actuators.^[1–4] Many of these soft devices consist of pneumatic or hydraulic-operated hyperelastic actuators that expand internal geometries to achieve multiaxis manipulation.^[5–7] A large portion of soft robots are operated with conventional fluids, such as air or water, and possess distinct deformation states based on pressure input and hyperelastic properties. Some approaches implement more complex behavior and memory using granular media to tailor expansion and rigidity.^[8] However, in nature, many biomechanical actuators transfer complex fluids between internal cavities for motion.^[9] For example, the hydraulic system of the “jumping-spider” arthropod produces rapid and explosive limb movement using shear-thinning transmission fluid. The pressure


distribution is controlled by the geometry of the limb and joint segments that direct the shear-thinning biofluid to move.^[10] Another biomechanical fluid system is the lymphatic system of tuna, which they use to orient their fins during high-performance swimming and maneuvering.^[11] At a slower scale, animals from the phylum mollusk use complex fluid and compliant bodies to locomote in various environments and surfaces. Gastropods such as snails and slugs use an undulating strategy and lubrication pressures with viscous Newtonian and non-Newtonian mucous to propel themselves.^[12,13] Moreover, one mollusk species uses a hemocoelic hydraulic system that acts as a hydrostatic skeleton for structure and motion.^[14] With many biological inspirations, one of the few hydraulic biomimetic devices researchers have developed is a soft robotic fish using Newtonian fluid, water, to induce caudal fin motion.^[5] Although, even with the biological motivations, few soft robotics have investigated complex fluids or, in our case, yield stress-induced flow for manipulating soft robotics. Here, our study addresses constructing and operating complex fluids using yield stress materials contained in soft robotic structures.

To fabricate the devices, we used 3D printing to encapsulate and produce functional hydraulic soft robotics. We use embedded 3D printing (EMB3D), an extrusion-based additive manufacturing method that can print with hyperelastic materials used in soft robotics. EMB3D supports the printed viscoelastic filaments in a suspension media avoiding yield stress-induced failure while enabling the creation of complex geometrical

J. K. Wilt,^[*] C. Coulais
Institute of Physics
University of Amsterdam
1098 XH Amsterdam, The Netherlands
E-mail: jacksonwilt@g.harvard.edu

J. K. Wilt, J. T. B. Overvelde
Autonomous Matter Department
AMOLF
1098 XG Amsterdam, The Netherlands

J. T. B. Overvelde
Institute for Complex Molecular Systems and Department of Mechanical Engineering
Eindhoven University of Technology
5600 MB Eindhoven, The Netherlands

 The ORCID identification number(s) for the author(s) of this article can be found under <https://doi.org/10.1002/aisy.202200332>.

^[*]Present address:

Lewis Lab
Harvard University
Pierce Hall 221, 29 Oxford Street, Cambridge, MA 02138, USA

© 2023 The Authors. Advanced Intelligent Systems published by Wiley-VCH GmbH. This is an open access article under the terms of the Creative Commons Attribution License, which permits use, distribution and reproduction in any medium, provided the original work is properly cited.

DOI: 10.1002/aisy.202200332

structures.^[15–17] The EMB3D process, also termed Freeform Reversible Embedding and Freeform Liquid 3D printing has successfully created soft robotic devices, mock organs, and thin-walled designs.^[18–25] For example, researchers used EMB3D to deposit fugitive sensory filaments into premolded soft robotic grippers. These filaments were either used as removable fugitive inks for internalized microfluidic channels or to measure deformation strain.^[26,27] However, few additive manufacturing techniques, including EMB3D, have intentionally retained the support materials for power transmission fluid in soft devices. One of the few techniques produced a quadruped robot using inkjet printing with noncuring liquid as a support material which retained polyethylene glycol as the non-Newtonian power transmission fluid.^[28] To build on previous work and integrate support fluid into actuation, we use the EMB3D process to exploit a hydrophobic yield stress medium retaining and sealing silicone actuators.

Using EMB3D, we introduce yield stress hydraulics to achieve shape memory in soft robotic actuation. In this fabrication process, we construct yield stress devices that exhibit shape retention properties, unintuitive expansion, and a deformation-dependent memory. Through our fabrication process, we retain the suspension material in the actuation channels and highlight the unique shape memory properties of a yield stress transmission fluid. Using the suspension transmission fluid directly after the printing phase further advances a workflow for untethered robotic operation and production in future research.^[29,30] Within the study, we exploit yield stress properties to create interconnected networks whose flow properties are determined by oscillatory rheology. The yield stress transmission fluid demonstrates shape retention and localized flow, advantageous in soft robotic actuating applications that require permanent deformation, and low energy input.^[31–34]

In turn, we encapsulate the yield stress suspension material made of oil and fumed silica creating sealed hydraulic devices. We then provide insight into the future of non-Newtonian soft robot transmission media by comparing the non-Newtonian fluid to Newtonian fluid actuation. We create multireservoir designs that test the flow of Newtonian and yield stress fluids across multiple fluid capacitors. The reservoir-based diagnostic structures test both the force transmission and the strain memory of each fluid by tracking the membrane and actuator deformation. Our gripper design combines the shape memory effects discovered with a three-reservoir design and observes shape memory in the arms of the bending actuators. In testing the diagnostic devices and gripper, we show that yield stress-operated devices are viable for shape retention properties and possess hysteresis in force recovery.

2. Results

2.1. Rheology of EMB3D Silicone Ink and Suspension

Our EMB3D approach uses nanoscale fumed silica particles suspended in heavy mineral oil, a technique investigated to produce a stable hydrophobic yield stress material.^[35] The resulting mineral oil and fumed silica (6 wt% fumed silica) material demonstrate a yield stress behavior. Such comparably low yield stress

reinforces suspension recoverability while allowing predictable deposition locations of an extruded silicone ink (**Figure 1a**). We print with platinum-curing silicones because of their fluidity at room temperature and postcure elasticity, which is ideal for soft robotic actuators. We tailor the silicone ink by mixing a soft silicone material Ecoflex 00-30 (Shore hardness 00-30) and a moderate hardness silicone material SE 1700 (Shore Hardness 48 A). This ink is selected because of its lower viscosity and intermediate curing temperature (70 °C for 4 h) while still in the suspension container. Its elastic properties, once cured (**Figure S3**, Supporting Information), combine the softness of Ecoflex with the robustness of SE 1700, which is ideal for our soft robotic application.

2.2. Producing Yield Stress Soft Robotics

The aspects of EMB3D with suspension encapsulation produce soft devices with few postprocessing steps, rapid turnaround, and tailorable transmission media. Once we created a viable ink–suspension relationship, we designed 3D models for the EMB3D fabrication. The digital model assigns the filament layer height, δh , and contains the vectorized G-code coordinates. We deposit the silicone ink in oil-silica suspension, which also recovers from the nozzle shear during print movements (**Figure 1b**). We produce soft devices with deformable membranes that are 3–4 layers thick, which are used as elastic energy storage in their strained states. The membranes connect to thicker conical reservoirs that store the bulk volume of the transmission fluid. The reservoirs compress to distribute the transmission fluid through the channels and connected reservoirs. Our more advanced diagnostic and gripper designs include constrictive channels that control the reservoir volume distribution into connected reservoirs. While we aim to study retained yield stress transmission media, we also benchmark our devices with Newtonian transmission media. The devices are evacuated and reinjected with pure mineral oil, where we gather data on Newtonian fluid actuation. To evaluate our process, we first test a simplified bending actuator to demonstrate channel integrity and fluid injection.

With the cured EMB3D devices, we demonstrate two forms of fluid transfer through fluid injection in self-contained reservoirs (**Figure 1c**). To validate the transfer process and provide actuators for initial testing, we produce an exemplar soft robotic gripper device through EMB3D. After creating the larger structure, we remove one bending actuator from the device (**Figure 1d**) to demonstrate the external injection process. For qualitative analysis, we use the finger actuator to measure the angular actuation from the mineral oil and fumed silica transmission fluid (**Figure 1e**; **Video S1**, Supporting Information). The finger is outfitted with a 10 cc syringe containing 4 cc of oil-silica 6 wt% material and injected into the finger actuator. After the injection pressure is released, the fluid media flows back 2 cc into the syringe and remains in this deformation state 1 min after recovery. The backflow recovery alleviates part of the stored elastic deformation from the actuator. With the partial recovery apparent after backflow, we design a reservoir-based device to investigate strain and force discrepancies between Newtonian and yield stress transmission fluid.

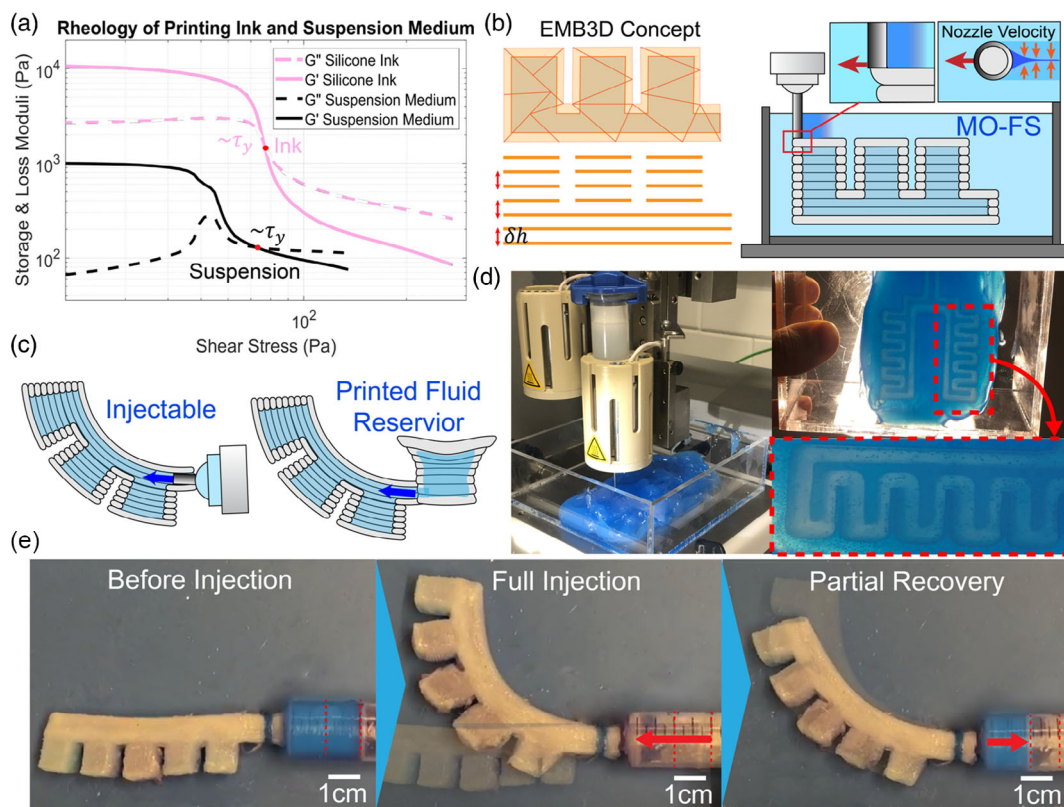


Figure 1. EMB3D using rheological values and digital designs to construct soft actuators. a) Dynamic mechanical behavior of the silicone ink and suspension medium. b) Diagram of the digital design to the G-code with print heights to the EMB3D process showing a recoverable suspension after nozzle shear. c) Comparing different post-process procedures associated with actuating the soft devices, including injection of fluid through an external reservoir or printing an internalized reservoir. d) The experimental setup of the printing apparatus and the underside of a printed geometry are still retained in the suspension. e) An EMB3D-produced finger actuator is injected from an external syringe with the oil-silica material first without injection, then with total volume displacement (2 cc) from the syringe, and finally, the partial recovery and backflow of fluid into the syringe.

2.3. Bireservoir Design: Force Transmission

We designed a diagnostic bireservoir soft device with two deformable membranes and reservoirs connected by a constrictive channel (Figure 2a). The bireservoir device is a compression testing setup to compare the suspension medium and Newtonian hydraulics stress–strain behavior. The constrictive channels connect and provide fluid flow to adjacent reservoirs, expanding the device membranes. The bireservoir demonstrates fluid rheology effects on force transmission and the hysteretic force during compression cycles of the yield stress fluid. The oil-silica fluidizes when being compressed and forced to flow between reservoirs. Due to the required repeat loading and unloading of our devices, we also outline the basic rules for creating multiuse sealed devices that are effective for our diagnostic and gripper geometries.

We used EMB3D fabrication to produce the sealed reservoir devices through layer-by-layer filament deposition. Our design contains high overhang angles and complex internal geometries, which exhibit the omnidirectional capabilities of EMB3D. However, we encountered challenges with interlayer adhesion which we confronted with layer height tuning. Here, the diagrams show that the overlap of printed devices is critical for

interlayer adhesion (Figure 2b,c). When using a spacing equal to the nozzle diameter of 0.84 mm, the oil-silica between layers inhibits the crosslinking (Figure 2b), causing insufficient layer bonding and subsequent delamination in the walls and membranes. To resolve this, we select a layer-to-layer distance of 0.53 mm using a 0.84 mm nozzle to produce a sufficient seal. Any greater filament distance and the devices consistently failed within one compression cycle. Using the 0.53 mm layer-to-layer distance, we create a sealed conical shell, thus producing a soft device with a deformable soft membrane (Figure 2c). The slicing parameters enable high overlap sealed devices: 1) the silicone membrane infill sealing was more successful at 200% of wall overlap where the infill is deposited two layers into the walls; 2) Sealed devices are more successful if each wall layer is printed first and succeeded by the infill or inner walls; 3) Large horizontal surface infills, such as the top and bottom layers, are generally more successful with three filament widths for the reservoir walls; and 4) The infill seal is more successful with rectilinear patterns that alternate pathing perpendicular from layer to layer. With a sufficient printing protocol, we construct devices containing Newtonian and yield stress fluid for force transmission.

The bireservoir compression measures critical shear forces and the local deformation from one reservoir to the adjacent

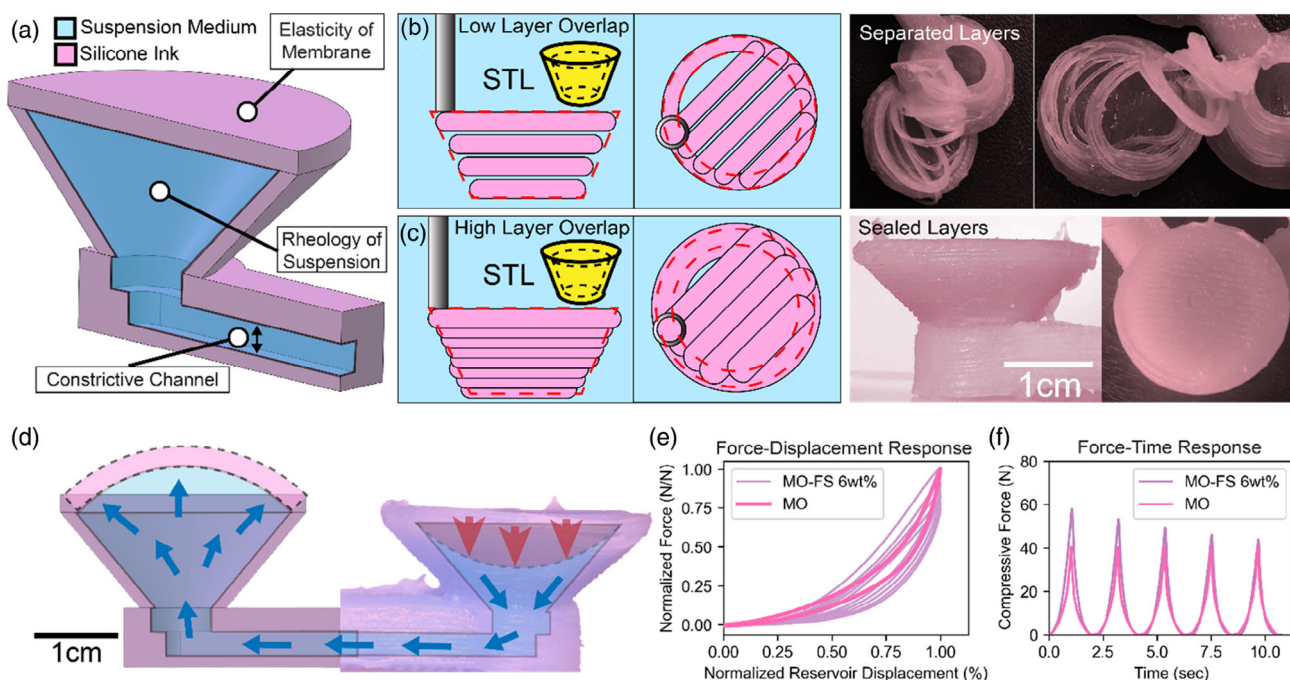


Figure 2. Concept and response of EMB3D biresevoir design with oil (MO) and oil-silica (MO-FS) fluids. a) A yield stress-operated device's key components include an elastic membrane, yield stress suspension rheology, and constrictive channels. b) The unsuccessful printing process for the biresevoir is indicated by delamination from the low layer overlap. c) Successful printing of the biresevoir device that contains the suspension fluid or other transmission media from high layer overlap. d) The biresevoir design demonstrates printed membrane deformation and fluid flow to the adjacent reservoirs. e) Force–displacement and f) force–time response of the biresevoir device over multiple compressions at 10 mm s^{-1} of a single reservoir comparing retained oil-silica and pure oil fluid.

reservoir (Figure 2d). We exploit the shear effects of restrictive channels and deformable membranes with non-Newtonian and Newtonian fluids. The compressive fluid flow is governed by the yield stress material properties and constrictive channels, with dimensions $3.3 \text{ mm} \times 2.2 \text{ mm}$ in the computer-generated model. The conical reservoir containing the bulk transmission fluid has a base radius of 12 mm , height of 12 mm , and capacity 1.8 cm^3 of volume. We entirely displace a single reservoir repeatedly for five cycles at 10 m s^{-1} using a cylindrical geometry (Figure 2e) and record the force of the compressed reservoir over the testing procedure. Compressing the membrane overcomes the critical yield shear stress of the oil-silica material to flow into adjacent reservoirs. Normalization is performed by dividing the maximum normal force from the force measurements during compression testing for each fluid type. The oil-filled design shows an increase in force with a hysteresis prominent in the displacements above 50% in the loading and unloading curves. When retaining the oil-silica medium, we observe a hysteresis, several factors larger than the pure oil inclusion. The oil-silica inclusion also possesses hysteresis upon the unloading cycle, which is more on initial compression and gradually decreases throughout testing. However, most importantly, the oil-silica force response progressively decreases to 76% of the maximum initial force by the end of the testing procedure. The hysteresis is due to the impeded flow of the viscous liquid, but hysteresis is still more significant in the yield stress material. The lower maximum force indicates stored elastic energy that could be in the form of membrane strain after fluid displacement.

The force–time response (Figure 2f) indicates the displaced fluid, which initially requires greater compressive force but progressively diminishes after five cycles. The higher forces required to actuate can be a negative consequence of the yield stress fluid by compromising the mechanical integrity of the device. However, the yield stress materials that restrict flow could also create the primary mechanism producing shape memory. Currently, these results show no shape memory, only recovery response. Our design can theoretically amplify the hysteresis and show shape memory by making channels more restrictive or membranes thinner. But to address this in our study, we increase the distance traveled in constricted channels by including multiple reservoirs connected in series through a triresevoir device.

2.4. Triresevoir Design: Localized Flow and Shape Retention

We developed a triresevoir design, 3D geometry (Figure 3a; 3D model 1, Supporting Information), and G-code (Figure 3b), analogs to a multireservoir soft robot using three capacitive reservoirs in one fluidic network. Our study conducts a sequential compression test cycle to view flow distribution and volumetric accumulation in the triresevoir device. Compressing the filled reservoirs causes shear stress to accumulate in the yield stress fluid in the constrictive channels. This shear stress build-up eventually surpasses the critical shear stress and fluidizes the yield stress material. We sequentially deform the reservoirs to gather the state memory through membrane forces and strain

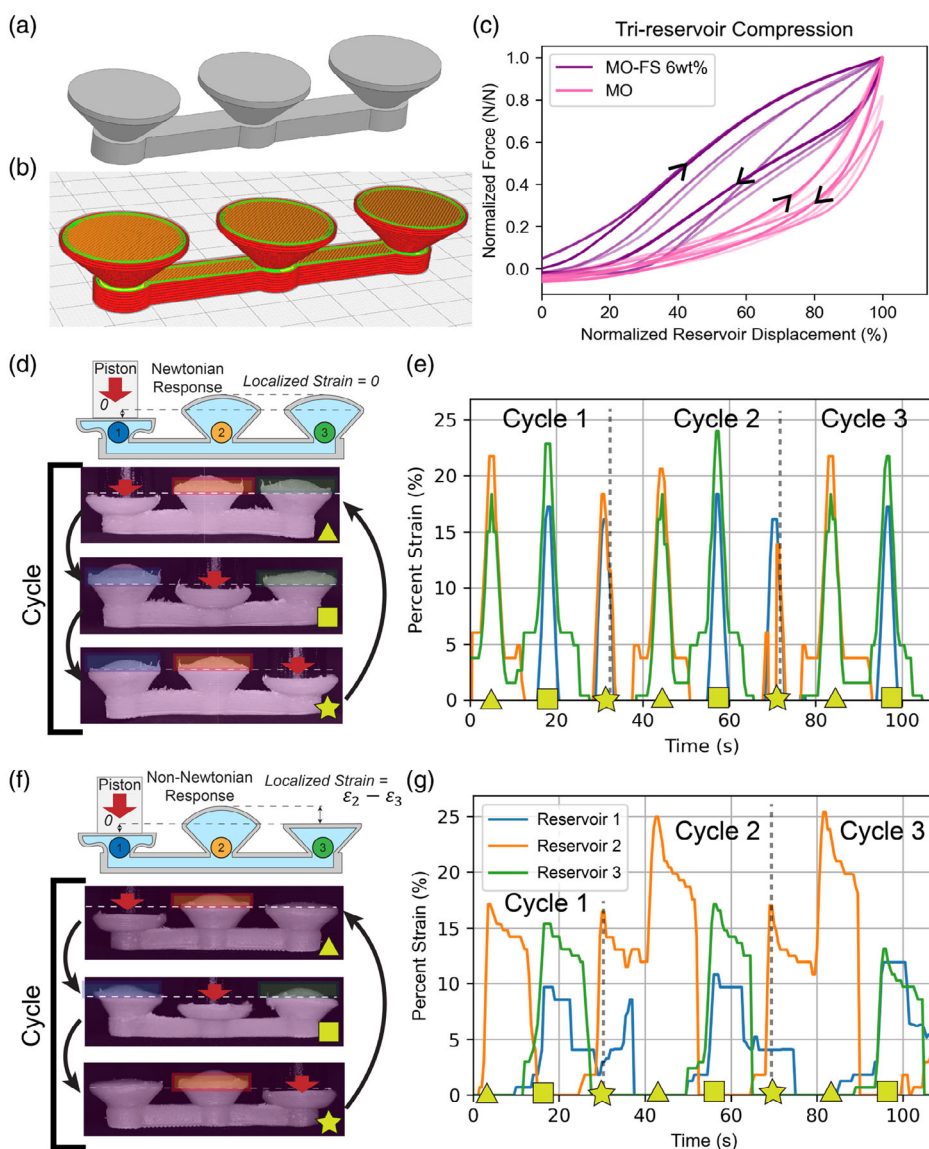


Figure 3. Rheology-dependent memory in the tri-reservoir device using sequential compression. a) 3D model of the tri-reservoir device and b) G-code pathing of the tri-reservoir device. Sequential compression results for oil-filled multi-reservoir devices. c) Initial force response of the oil and the oil-silica fluid expansion. d) Sequential compression results for oil-filled tri-reservoir device e) with the rapid response of strain values relative to the cap height. f) Sequential compression results for oil-silica filled tri-reservoir device g) with strain responses showing partial strain memory plateaus.

after the fluidized transmission fluid recovers. We calculate strain as h/h_0 representing h_0 as the undeformed height of the conical reservoir based on the digital design 1 cm and h as the height of the final reservoir diagnostic design. The tri-reservoir design shows that during a three-compression cycle (Figure 3c), the oil fluid has less hysteresis and lower normalized force as compared to the oil-silica fluid. In contrast, the oil-silica system has a higher normalized force and a more linear stress-strain response implying elastic characteristics. These force response curves for the oil fluid are similar to that of the bi-reservoir design. However, the strain for the yield stress in the tri-reservoir is much different with nonlinearly distributed normal forces during testing. The unique normal force response

highlights that the fluid-structure interaction depends on the design channel interconnectivity.

Sequential compression cycles show the relationship between strain memory and membrane deformation. Cycles are performed on the tri-reservoir design containing oil and the oil-silica material. We perform three cycles to track shape memory for each fluid-filled device where one cycle compresses reservoirs #1, #2, and #3 (three stages denoted by the yellow triangle, square, and star, respectively). The Newtonian strain response is shown diagrammatically (Figure 3d), going through one cycle of compressions and showing membrane strain from an unactuated state. The strain response of the oil transmission fluid recovers on the order of 2 s with no shape retention plateaus

(Figure 3e). We measure a minor strain of 5% in the two uncompressed reservoirs with a maximum strain range of 18–24% in fully expanded membranes. The high expansion and return to an unstrained state confirm the full recovery expected from a Newtonian system. This response is expected as the design has low shear-dependent properties in adjacent and far-field reservoirs. In contrast, when using the yield stress fluid, we expect that there will be a more asymmetric flow in the multireservoir device.

To test this, we perform the compression cycle (Figure 3f) using the oil-silica yield stress fluid, which produces a strain plateau (Figure 3g) after the peak strain. The first stage (denoted by the yellow triangle) includes a strain profile with only expansion on membrane #2. Then by compressing reservoir #2 (denoted by the yellow square) the flow is transferred to both adjacent reservoirs, however, creates more prominent strain in reservoir #3. The #3 reservoir is compressed (denoted by the yellow star), where reservoir #2 reaches a strain of 17%, but over 15 sec, the membrane returns to 13–14% strain. The 13–14% strain represents the approximate recovered strain plateau and is the essence of strain memory. After the initial cycle, the second and third cycles have similar strain results for all membranes. Here, the system also demonstrates a memorized secondary state with a higher strain at the membrane after the first cycle. A single strain plateau appears at the first compression, and subsequent compressions create two strain plateaus at a greater initial strain response of 24% and recover to 19–20%. The sequential compression process shows a replicable system state retention after the first cycle. This simple experiment demonstrates that we can exploit this system state to exert a task to retain a strain plateau according to the yield stress structure relationship within a soft body, so we design a more complex device representative of other soft robotics.

2.5. Yield-Stress-Operated Gripper

We finally fabricate a soft gripper to investigate how the yield stress enables shape memory consistency for shape retention after actuation (3D model 2, Supporting Information). We create a yield stress-operated soft gripper connecting two bending robot actuators with a central reservoir. The gripper model is created in SolidWorks (Dassault Systemes SOLIDWORKS Corp.) (Figure 4a,i) and vectorized in G-code (Figure 4a, ii). The device is EMB3D printed in the oil-silica fluid suspension (Figure 4a, iii and iv; Video S2, Supporting Information), enabling the high overhangs and encapsulating properties necessary for the soft gripper design. The gripper actuation (Figure 4a,v) demonstrates the angular deformation from a yield stress fluid inclusion, the oil-silica 6 wt% suspension. We compress the oil and oil-silica-filled reservoir using 10 mm s^{-1} displacement of a trapezoidal reservoir for angular actuation of the bellows. The reservoir was fully evacuated by displacing a trapezoidal fixture, found in Supplementary Information, into the full depth, 25 mm, of the trapezoidal reservoir. We also use the gripper device to drag an object (Rubik's cube) under a fully compressed trapezoidal reservoir (Figure 4b; Video S3, Supporting Information) across a PVC sheet. This confirms its ability to act as a standard gripper while being powered. We then record

the compressive forces when displacing the reservoir of an unobstructed gripper. The normalized compressive force (N/N) has lower hysteresis levels for the oil fluid, while the oil-silica has more pronounced force and hysteresis between the loading and unloading cycles (Figure 4c). The oil-silica gripper encounters more force drops in the response curve, likely due to intermittent fluid flow through the restrictive cross-sections. The design with the oil-silica also experiences a force peak near 60% strain that indicates more constrictive flow, likely from a trapped air bubble that is bypassed in further compressions. The force hysteresis found in the bireservoir tests is a property inherent to the geometry of the gripper device, which is also characteristic of the force response in the trireservoir device. After confirming unique hysteresis, we evaluate if the shape memory found in the trireservoir is also detected in the gripper design.

We compress the center gripper reservoir at 10 mm s^{-1} using the 3D-printed trapezoidal geometry fixed to the compression tester, which delivers the transmission fluid into the soft robot arms. We observe shape memory over time using the angles of the rectangular bellows of the gripper. We track the angular deflection of each gripper actuator by measuring the angles at each bellow, θ , over the experiment measurement time, 410 s for oil and 650 s for oil-silica. We track the deflection strain using a grayscale line with the bellow angle closest to injection denoted as the light-gray line and the furthest bellow angle as black (Figure 4d). The bellows of the unmodified oil demonstrates a rapid response with distinct strain peaks (Figure 4e) between reservoir loading and unloading. The unstrained gripper (Figure 4e) in blue-highlight is fully compressed (Figure 4e) in red-highlight, but recovers after compression is released and the fluid returns to the reservoir. Gripper strain response (Figure 4e) has an inset that includes the comparable angular differences between bellow pairs starting with the b_0 , or bellows closest to the injection site, and b_4 , which is at the end of the actuator. This inset contains the strain value difference represented by a linearly increasing difference from the first to second bellows b_0 - b_1 up to the largest strain difference at 8° between the b_3 - b_4 pair, respectively. The angular change is lower in the bellows adjacent to the injection site for the Newtonian fluid, which we assume is due to the geometry of the walls near the fluid entrance to the actuator arm. However, the angular change also shows an average angular deviation of 8° between the end bellows, indicating equivalent flow to the adjacent reservoir. After the compressions, the bellows fully recover to their unstrained shape at nearly 0° and perform a similar actuation profile in subsequent tests. The low shape retention and rapid recovery in Newtonian actuation coincide with the trireservoir device, but we also aim to test yield stress media in the same actuator.

Testing the oil-silica yield stress fluid inclusion results in shape retention properties after its initial actuation (Figure 4f). We show the experimental sequence of compression for the unstrained gripper (Figure 4f) in blue-highlight, partially retained shape state (Figure 4f) in yellow-highlight, and fully actuated (Figure 4f) in red-highlight, which is a strain response unique to the yield stress inclusion. The (Figure 4f) inset shows maximum angular strain between the bellows has a nonlinear change in the sequence of bellows pairs. The pairs b_1 - b_2 and b_2 - b_3 have the same angular difference, evident of nonlinear

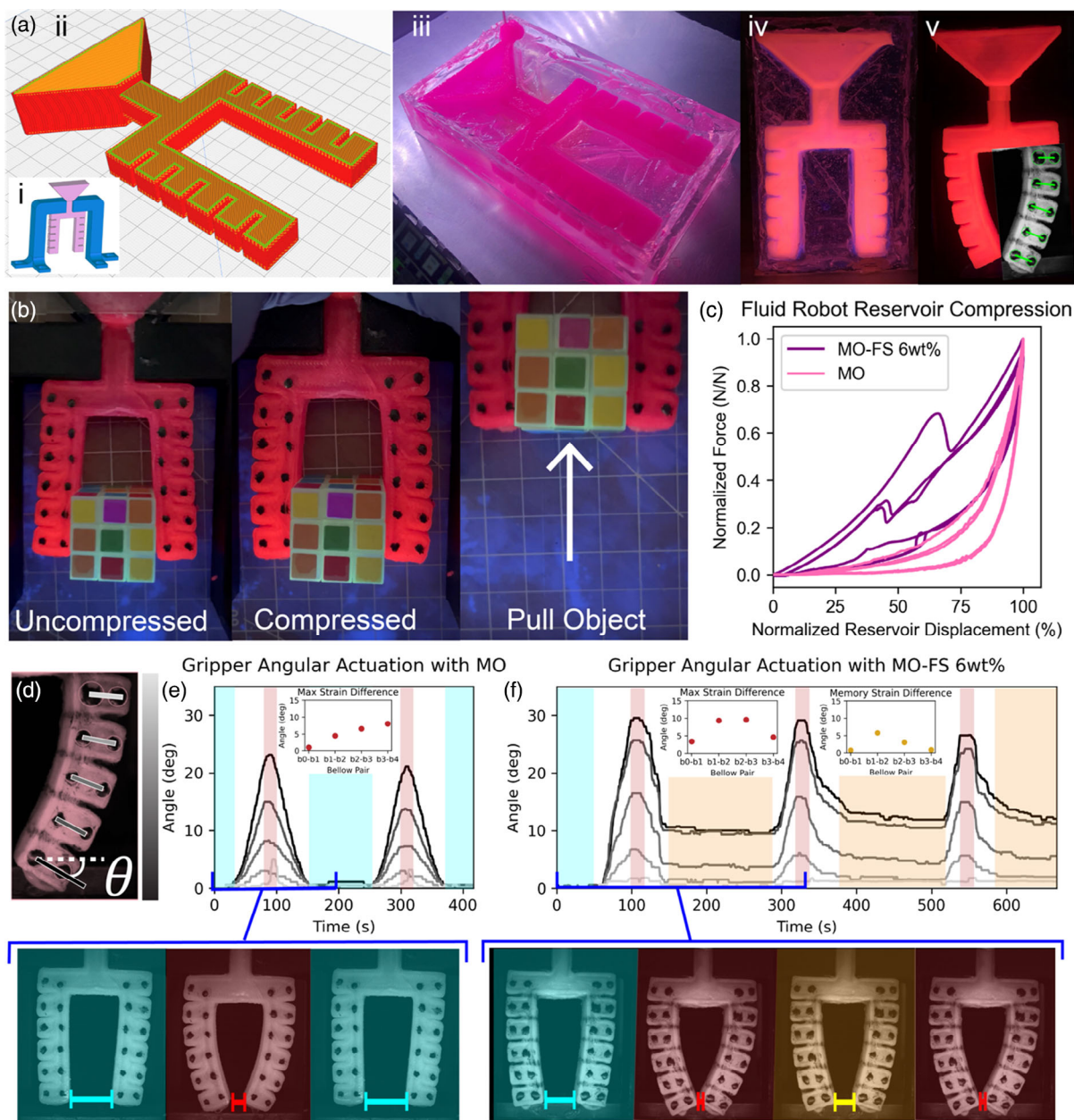


Figure 4. Gripper design operated by oil (MO) and oil-silica (MO-FS) 6wt%. a) Full process of encapsulated EMB3D for soft robotics involving (i) computer-aided design, (ii) G-code slicing, (iii) fabrication, (iv) post-cured EMB3D device in blacklight, and (v) encapsulated soft robot gripper fully actuated with an example of the computer vision analysis for tracking. b) Sequence of compression-induced actuation of the gripper device used to pull a Rubik's cube. (c) Normalized force-displacement response of the gripper reservoir while being actuated using MO and MO-FS fluid. d) Angular values of the gripper actuator using θ of each bellow with respect to the horizontal axis. e) Angular change of gripper bellows during actuation for the oil-filled design, and f) the oil-silica transmission fluid. Each actuation denotes the unactuated gripper with blue-highlight, shape memory actuation with yellow-highlight, and the full actuation with red-highlight.

fluid flow within the actuator compared to the oil fluid. With the yield stress fluid, the end bellows shows the lower value of end-bellow angular change of 5° from the peak of the previous bellows. The yield stress fluid shows an equal distribution of deformation where the angular change exhibits similar values at 10° . The middle bellows have a deformation at approximately 4° – 6° regardless of the subsequent compressions. The 10°

angular difference between the middle bellows becomes the system's steady-state value until, theoretically, the fluid from these areas shears back into the trapezoidal reservoir. The strain memory is only present in the silica-oil actuation fluid and is represented in the corresponding (Figure 4f) inset. The continuous strain memory produces a memorized angular difference at $b1$ - $b2$ and $b2$ - $b3$ and a low difference due to a lack of flow at

the *b3-b4* pair. When observing the oil-silica transmission fluid flow, there are less pronounced angular deflection peaks, insinuating a slower response time across all bellows. The compression testing showed distinct actuation profiles at full compression due to localized flow from the yield stress effects and more significant end actuator extension from the Newtonian fluid. The smaller deflection of the end-bellow from the oil-silica gripper insinuates prominent restrictive flow along the yield stress actuator. The oil actuator experienced more significant expansion at the end of the actuator, and the oil-silica experienced more pronounced deformation at the injection site and memorized bending strain. Because of the localized expansion at the injection site, the gripper can close with less fluid injection, potentially creating a more efficient closing mechanism.

3. Conclusion

We show yield stress-operated soft robotics are a promising avenue for shape memory and force hysteresis. We use EMB3D as our fabrication to successfully produce our sealed yield stress-operated soft robotics by encapsulating the support suspension as the transmission media. Our approach sacrifices higher quality to rapidly iterate on the novel printing framework with economical materials and equipment. Our interconnected bire-servoir device shows full strain recovery with yield stress and Newtonian transmission fluid with a pronounced force hysteresis in the yield stress devices. Our trireservoir design allows the flow to nonadjacent reservoirs while showing intercycle memory of yield stress-operated systems. We see a strain peak and subsequent strain plateau with the oil-silica, and the deformation state resets during sequential compressions. The gripping actuator demonstrates the complete recovery and more uniform angular deformation using a Newtonian fluid with localized and memorized angle change using the yield stress material. A significant finding is that we can see similar force response curves for oil-filled devices but more complex geometry-to-rheology relationship force responses for oil-silica yield stress material. The novelty of this actuation and fabrication process might enable the design of actuators in contexts where the constant application of pressure is impractical. For example, biomedical or chemical applications that need prolonged contact with surfaces but minimal forces even after removing the power source. Shape memory properties can also be advantageous in applications where actuators are deformed to retain conformality. Applications spanning manufacturing manipulation to biomedical actuators can utilize the localized flow and shape retention as valve frameworks or shape memory grasping arms. In the biomedical field, yield stress deformation can be used to conform and retain the shape of organic shapes and surfaces. Printing with functional yield stress components can be integrated into more complex 3D devices providing a shape memory avenue for suspension printing of functional devices. Notably, our yield stress-operated robot technology and partial shape retention are most promising for low-energy input in robot grasping and medical devices that require tunable shape memory. In the future, more quantitative results on the integrity of printed structures would translate the work into more applications.

4. Experimental Section

EMB3D Hardware Framework: The 3D printing apparatus that we used was the Hyrel ENGINE SR (Hyrel, Norcross, GA) which is an open-source modular fabrication platform. The print process used a high-torque volumetric displacement print head SDS-030XT (Hyrel, Norcross, GA) to print with disposable 30 cc syringes. The syringes were outfitted with an 18 gauge 1.5 inch 840-micron nozzle (Nordson Corporation, Westlake, OH). We use the Ultimaker Cura 4.7 software to perform G-code slicing on the 3D-modeled devices (STL files). Once again, layer heights were set at a layer-to-layer distance of 0.53 mm using a 0.84 mm nozzle that produced a sufficient seal for fluid inside the object. The STL models can be obtained from the Supplementary Information Files.

Suspension Fluid Formulation: The suspension fluid consisted of nanoscale-fumed silica particles (FS) dispersed in heavy mineral oil (MO) which was placed into the EMB3D printing vats. The maximum amounts mixed at one time were 75 g MO and 4.8 g FS (6 wt% of mixture weight), and Electric BlueTM (Smooth-On Inc., Macungie, PA) fluorescent silicone pigment of 0.5 g was mixed using a planetary shear mixer (Dispermill, Almere, NL), also known as a dual-axis centrifugal mixer. The mixing setting used for the first stage was approximated at a 1400 rpm mixing rotation rate and 280 rpm centrifugal mixing rotation rate for 90 s. This mixture was then removed from the shear mixer, the sides of the container were scraped to integrate the unmixed FS, and finally remixed using the initial parameters setting. Next, the suspension fluid was placed into the EMB3D printing vats. Vats consisted of cast acrylic panels that were cut using a commercial laser cutter and assembled using Acrifix 117 to bond the panels together, creating rectangular vats. To place the fluid special FDM, 3D printed designs were used to climate the gas voids during the mixing container-to-vat transfer process. We FDM print a disc design with the same diameter as the mixing container with a center hole the diameter of the injection syringe. We then use the injection syringe comprised of a 30 cc disposable syringe cut at the 0 cc gradation line to press the FS-MO matrix into the suspension vat. The other design consisted of a thin rectangular plate design with a center hole that coincides with the bottom of the vat. The MO-FS-filled syringe was used to iteratively inject enough material in the vats depending on the size of the vat, contained 100–250 cc of FS-MO material, and is filled following an injection process (Figure S1, Supporting Information).

Silicone Ink Formulation: The EMB3D inks were mixed, placed in a syringe (Figure S2a, Supporting Information), and printed (Figure S2b, Supporting Information) using common commercial platinum-curing silicone materials. The softer silicone material used was Ecoflex 00-30 (Smooth-On Inc., Macungie, PA). The more rigid silicone with hardness Shore 48 A was SE1700 (Dow Inc., Midland, MI). The ink used for all soft devices was mixed using the planetary shear mixer and was constructed for its favorable flow properties, extended pot life, and final mechanical properties. The Ecoflex and SE1700 precursors were mixed to possess intermediary properties between the unmodified silicone properties. The final ink consisted of a 15 g of SE1700 mixed with 1.5 g of the SE1700 catalyst and Electric PinkTM (Smooth-On Inc., Macungie, PA) fluorescent silicone pigment of 0.3 g. The first combination was mixed with a centrifugal rotation of 1400 rpm and a mixing rotation of 280 rpm. Finally, 7.5 g Part A Ecoflex 00-30 and 7.5 g Part B Ecoflex 00-30 were added. In quick succession, 0.9 g of cure retarder, SLO-JO, was added to the mixture. The excess cure retarding agent was added that extends the pot life of the material to be used much longer than the prescribed 30-min pot life of the EcoFloex 00-30. The prescribed maximum amount of cure retarder is 2 wt% to Part B of Ecoflex. However, in our ink, the cure retarder represented 12 wt%, likely affecting the final mechanical properties. We ignored these potential effects to engineer printable ink, which could be optimized in future studies. Our approach created a latent curing silicone ink with flexible properties and was cured through a heating process.

Postprocessing: The heating and postprocessing of the EMB3D structures are necessary to fully cure the encapsulated designs. First, the devices were placed in an oven at 70 °C for 4 h which exceeds the required amount of precuring time but is necessitated by the size and amount of oil surrounding the encapsulated structures to ensure uniform

heating and a sufficient crosslinking. Next, the EMB3D devices were removed from the suspension baths and cleaned with ethanol and paper towels to remove the external suspension fluid. The EMB3D parts were then postcured at 100 °C for 30 min. The devices were allowed to cool for 30 min to allow the internal fluid to be tested at near-room temperature reducing the chance that the temperature will affect viscosity. The suspension fluid was then deaerated, and any solid particulate was removed. The suspension was reusable indefinitely as long as the solution remains free from significant solid waste particulates.

Mechanical Testing of Printed Silicone: The mechanical response of EMB3D silicone components is important for future 3D-printed soft robotic devices. We test the printed materials to understand the influence oil-based media diffusion into prepolymer filaments, and interstitial oil-filled voids have on the final mechanical properties. The 50/50 mixture was selected because of its commonality in the soft robotics fields and acceptable final mechanical properties. The geometry used for tensile specimens was derived from the ASTM standard D412 (3D model 3, Supporting Information) elastomeric material testing procedure and printed using DIW (Figure S3a, Supporting Information) and EMB3D (Figure S3b, Supporting Information). Here, we show a comparison of a conventionally printed geometry according to cast, DIW, and EMB3D, after the curing process. We also explored different nozzle sizes which were denoted as 0.532, 0.654, and 0.784 mm; however, we select 0.84 mm for all devices because of its ease of extrudability.

One print configuration is tensile-tested where the direction of print lines is perpendicular to that of the axis of strain which is also the angle of strain occurring in the soft devices when expanded or compressed. The testing procedure shows that the greatest tensile strain without critical failure of the cast component is much greater than that of the conventional EMB3D of the same formulation. The ultimate tensile strain is up to $\approx 250\%$ for conventional DIW and cast components but $\approx 100\%$ for the EMB3D (Figure S3c, Supporting Information). The DIW-printed devices also show several drops in stress due to delaminating filaments of the aggregate structure. We find the surface effects of the printed samples, mainly surface roughness, are less apparent in the DIW, which we predict is due to gravity and surface tension-induced coalescence. The lower mechanical properties of the EMB3D specimen are likely due to surface roughness and retained interstitial suspension fluid microvoids causing stress concentrations.

Compressing Fluid-Filled Devices: The devices in the study were compressed using an Instron 5943 test frame using a 500 N load cell. All tests gathered force data at a strain rate of 10 mm s^{-1} and using custom-built test setups (Figure S4, Supporting Information). Two testing geometries were used for compressing the devices. The fluid-filled devices used 3D-printed frames that aligned them with each testing geometry (3D model 4, Supporting Information). One was a cylindrical geometry used to compress the conical reservoirs that were 24 mm in diameter (3D model 5, Supporting Information), which were fixed to the top vices of the Instron test frame (3D model 6, Supporting Information). While mounted, the other trapezoidal geometry (Figure S5a, Supporting Information; 3D model 7, Supporting Information) was used to compress the trapezoidal gripper reservoir (Figure S5b, Supporting Information; 3D model 3 and 3D model 8, Supporting Information). All of the testing devices can be found in STL format in the Supporting Information files.

Supporting Information

Supporting Information is available from the Wiley Online Library or from the author.

Acknowledgements

J.K.W. was supported by the U.S. Fulbright Student Program and the Netherland America Foundation. C.C. acknowledges funding from the European Research Council under Grant Agreement 852587. This work is part of the Dutch Research Council (NWO) and was performed in part at the research institute AMOLF.

Conflict of Interest

The authors declare no conflict of interest.

Data Availability Statement

The data that support the findings of this study are available in the Supporting Information of this article.

Keywords

3D printing, rheology, shape memory, soft robotics, yield stress

Received: January 25, 2023

Published online:

- [1] E. Siéfert, E. Reyssat, J. Bico, B. Roman, *Nat. Mater.* **2019**, *18*, 24.
- [2] S. Coyle, C. Majidi, P. LeDuc, K. J. Hsia, *Extreme Mech. Lett.* **2018**, *22*, 51.
- [3] C. Majidi, *Adv. Mater. Technol.* **2019**, *4*, 1800477.
- [4] C. Majidi, *Soft Rob.* **2014**, *1*, 5.
- [5] R. K. Katzschmann, A. D. Marchese, D. Rus, in *Experimental Robotics. Springer Tracts in Advanced Robotics* (Eds: M. Hsieh, O. Khatib, V. Kumar), Vol. 109, Springer, Cham, **2016**, pp. 405–420, https://doi.org/10.1007/978-3-319-23778-7_27.
- [6] J. T. B. Overvelde, T. Kloek, J. J. A. D'Haen, K. Bertoldi, *Proc. Natl. Acad. Sci. U. S. A.* **2015**, *112*, 10863.
- [7] P. Rothemund, A. Ainla, L. Belding, D. J. Preston, S. Kurihara, Z. Suo, G. M. Whitesides, *Sci. Rob.* **2018**, *3*, article no. eaar7986.
- [8] S. E. Bakarich, R. Miller, R. A. Mrozek, M. R. O'Neill, G. A. Slipper, R. F. Shepherd, *Adv. Sci.* **2022**, *9*, 2104402.
- [9] C. Liu, Y. Wang, L. Ren, L. Ren, *J. Bionic Eng.* **2019**, *16*, 367.
- [10] C. Göttler, G. Amador, T. van de Kamp, M. Zuber, L. Böhler, R. Siegwart, M. Sitti, *Soft Matter* **2021**, *17*, 5532.
- [11] V. Pavlov, B. Rosental, N. F. Hansen, J. M. Beers, G. Parish, I. Rowbotham, B. A. Block, *Science* **2017**, *357*, 310.
- [12] B. Chan, N. J. Balmforth, A. E. Hosoi, *Phys. Fluids* **2005**, *17*, 113101.
- [13] M. Denny, *Nature*. **1980**, *2*, 160.
- [14] B. G. Szymik, R. A. Satterlie, *Invertebr. Biol.* **2017**, *136*, 290.
- [15] Y. Cheng, K. H. Chan, X. Wang, T. Ding, T. Li, X. Lu, G. W. Ho, *ACS Nano* **2019**, *13*, 13176.
- [16] M. Schaffner, J. A. Faber, L. Pianegonda, P. A. Rühls, F. Coulter, A. R. Studart, *Nat. Commun.* **2018**, *9*, article no. 878.
- [17] C. S. O. Bryan, A. Brady-mine, C. J. Tessmann, A. M. Spatz, T. E. Angelini, *Soft Matter* **2021**, *17*, 3886.
- [18] Z. Wang, B. Zhang, W. Cui, N. Zhou, *Macromol. Mater. Eng.* **2022**, *307*, 2100813.
- [19] C. S. O'Bryan, T. Bhattacharjee, S. Hart, C. P. Kabb, K. D. Schulze, I. Chilakala, B. S. Sumerlin, W. G. Sawyer, T. E. Angelini, *Sci. Adv.* **2017**, *3*, article no. e1602800.
- [20] A. McCormack, C. B. Highley, N. R. Leslie, F. P. W. Melchels, *Trends Biotechnol.* **2020**, *38*, 584.
- [21] S. Abdollahi, E. J. Markvicka, C. Majidi, A. W. Feinberg, *Adv. Healthcare Mater.* **2020**, *9*, 1901735.
- [22] J. Zhao, N. He, *J. Mater. Chem. B.* **2020**, *8*, 10474.
- [23] T. Hinton, A. Hudson, K. Pusch, A. Lee, A. W. Feinberg, *ACS Biomater. Sci. Eng.* **2016**, *2*, 1781.
- [24] A. K. Grosskopf, R. L. Truby, H. Kim, A. Perazzo, J. A. Lewis, H. A. Stone, *ACS Appl. Mater. Interfaces* **2018**, *10*, 23353.

- [25] T. Calais, N. D. Sanandiya, S. Jain, E. V. Kanhere, S. Kumar, R. C. Yeow, P. Valdivia, *ACS Appl. Mater. Interfaces* **2022**, *14*, 230.
- [26] R. L. Truby, M. Wehner, A. K. Grosskopf, D. M. Vogt, S. G. M. Uzel, R. J. Wood, J. A. Lewis, *Adv. Mater.* **2018**, *30*, 1870106.
- [27] M. Wehner, R. L. Truby, D. J. Fitzgerald, B. Mosadegh, G. M. Whitesides, J. A. Lewis, R. J. Wood, *Nature* **2016**, *536*, 451.
- [28] R. Maccurdy, R. Katzschmann, Y. Kim, D. Rus, in *Proc. - IEEE Int. Conf. Robot. Autom.*, IEEE, June **2016**, pp. 3878–3885, <https://doi.org/10.1109/ICRA.2016.7487576>.
- [29] S. I. Rich, R. J. Wood, C. Majidi, *Nat. Electron.* **2018**, *1*, 102.
- [30] M. Vázquez, E. Brockmeyer, R. Desai, C. Harrison, S. E. Hudson, in *Conf. Hum. Factors Comput. Syst. - Proc. 2015*, ACM April **2015**, pp. 1295–1304, <https://doi.org/10.1145/2702123.2702569>.
- [31] A. Z. Nelson, K. S. Schweizer, B. M. Rauzan, R. G. Nuzzo, J. Vermant, R. H. Ewoldt, *Curr. Opin. Solid State Mater. Sci.* **2019**, *23*, 100758.
- [32] R. H. Ewoldt, *Soft Rob.* **2014**, *1*, 12.
- [33] A. Z. Nelson, R. H. Ewoldt, *Soft Matter* **2017**, *13*, 7578.
- [34] H. Wang, M. Totaro, L. Beccai, *Adv. Sci.* **2018**, *5*, 1800541.
- [35] Y. Jin, K. Song, N. Gellermann, Y. Huang, *ACS Appl. Mater. Interfaces* **2019**, *11*, 29207.